ORIGINAL ARTICLE



Printability study of self-supporting graphene oxide-laponite nanocomposites for 3D printing applications

Manish Sakhakarmy ¹ · Siyu Tian ^{1,2} · Lily Raymond ¹ · Guoping Xiong ^{1,2} · Jihua Chen ³ · Yifei Jin ¹

Received: 25 October 2020 / Accepted: 5 March 2021 / Published online: 13 March 2021 © The Author(s), under exclusive licence to Springer-Verlag London Ltd., part of Springer Nature 2021

Abstract

Graphene, a two-dimensional (2D) carbon allotrope, has been widely used in various fields due to its excellent inherent properties. Graphene and its derivatives usually possess poor printability, which makes it challenging to create three-dimensional (3D) structures. The objective of this work is to investigate a nanoclay-assisted 3D printing approach to print 3D structures from self-supporting graphene oxide (GO)-laponite nanocomposites. Due to the physical crosslinking between nanoclay and GO, the resulted nanocomposites can be directly printed into complex geometries in air. A significantly large range of laponite to GO mass ratio (5.00 to 32.00) was achieved by a mixing and centrifuging method as compared to previously reported GO-laponite composites made by the solvent evaporation method. It is found that the concentrations of nanoclay additives and GO can significantly affect the extrudability. In addition, the formability of the extruded filaments was studied by assessing the filament shapes/dimensions as well as the filament deflections when printing between supporting structures. Our results show that operating conditions such as dispensing pressure, path speed, nozzle diameter, and stand-off distance can be used to control the width of printed filaments on a substrate. Due to the self-supporting property of the proposed GO-laponite nanocomposites, it is possible to form continuous filaments with negligible deflections between supporting structures. Thus, 3D scaffolds with well-defined shape and controllable geometries have been successfully fabricated, which proves the proposed nanoclay-assisted 3D printing technology to achieve complex 3D graphene structures is feasible.

Keywords Graphene oxide · Nanoclay · Printability · Self-supporting · 3D printing

1 Introduction

Graphene, a two-dimensional (2D) carbon allotrope with sp² hybridization and a densely packed honeycomb lattice [1], has been heavily studied in recent years. Due to its excellent inherent electrical, mechanical, optical, and thermal properties, graphene and its derivatives have been widely used for various applications such as energy storage, sensing, mechanical damping, photo-detectors, and thermal insulation [2–6].

- Department of Mechanical Engineering, University of Nevada Reno, Reno, NV 89557, USA
- Department of Mechanical Engineering, The University of Texas at Dallas, Richardson, TX 75080, USA
- Oak Ridge, TN 37830, USA
 Center for Nanophase Materials Sciences, Oak Ridge National Lab, Oak Ridge, TN 37830, USA

Traditional methods and 3D printing techniques are two different strategies that have been utilized to fabricate 2D and 3D graphene structures. Traditional methods include hydrothermal [7–9], freeze-casting [10–12], chemical reduction [13, 14], and chemical vapor deposition [15], which all have several limitations, such as the low resolution of fabricated parts and inefficiency in the fabrication of large and complex 3D structures. Fortunately, the development of 3D printing provides a powerful tool to overcome these challenges. Of seven 3D printing techniques [16], material extrusion is widely used due to its easy implementation, low cost of processing, wide range of material selection, and high efficiency [17]. Fused deposition modeling (FDM) and direct ink writing (DIW) are the two main categories of material extrusionbased 3D printing. In FDM, solid polymer fibers such as polylactic acid (PLA) [18] and acrylonitrile butadiene styrene (ABS) [19] are used as build materials. These fibers are fed into printhead with a working temperature higher than the melt temperatures and extruded out to form continuous melt filaments. Due to a low ambient temperature, the extruded



filaments rapidly solidify with sufficient mechanical strength to hold subsequently deposited filaments. For 3D printing graphene structures via FDM, graphene particles must be mixed with matrix polymers [20] first to prepare composite polymer fibers, which complicates the pre-printing process and constrains the selection of matrix polymers. In addition, the high temperature during the preparation of composite polymer fibers, as well as the FDM-based 3D printing process, may deteriorate the intrinsic properties of graphene [20], which limits this method in 3D graphene structure fabrication. DIW is different from FDM such that the liquid build materials, like suspensions and/or solutions, are used as "inks." These inks are extruded through printhead to form continuous filaments, rapidly solidified via different crosslinking mechanisms (either physical [21-23] or chemical [24-26]), and 3D structures are constructed in a layer-by-layer manner [27]. Since it is unnecessary to prepare composite polymer fibers before printing, the technical challenges in FDM can be conquered by using DIW for graphene printing.

The primary requirement of DIW is the suitable printability of ink materials, which is defined by two methods: extrudability and formability. Extrudability is the capacity of extruding continuous filaments out of the dispensing nozzle, and formability is the capacity of forming filaments with controllable shape, dimension, and deflection after deposition. To improve the extrudability of graphene and its derivatives such as graphene oxide (GO), two methods have been used including (1) increasing graphene or GO concentrations and (2) adding additives as binders and/or viscosifiers. For the former, GO concentration has been increased to 13.3 mg/mL to facilitate the 3D printing process as reported in prior work [28, 29]. For the latter, various polymers [30, 31] and particle additives [32] have been investigated. For example, Garcia-Tuno et al. [33] added branched copolymer surfactant and gluconic--lactone into GO and successfully fabricated scaffolds; however, this process required an additional high-temperature reduction treatment to decompose the additives. Thus, the printed structures after reduction usually had poor density and mechanical properties. Similarly, Zhu et al. [32] added silica into GO suspensions to tune the rheological properties. In their studies, the isooctane bath was used to support the printed structures and prevent dehydration during printing, which makes the fabrication process complicated. Besides, additional treatments such as carbonization at high temperatures and etching were required, which may weaken the mechanical stiffness of printed structures. Yao et al. [34] prepared concentrated GO suspensions via a time-consuming redispersion process and mixed polymer and inorganic nanoparticle additives together to prepare a graphene-based ink. Their results showed that these additives ultimately weakened the mechanical properties, reduced the electrical conductivity, and required tedious post-processing for etching. Jakus et al. [35] demonstrated the printing of a composite consisting of polylactide-co-glycolide (PLG) and graphene dissolved into dichloromethane (DCM). However, rapid evaporation of DCM must be guaranteed in their study to form self-supporting filaments and prevent the deformation and/or collapse of the printed structures. To summarize, current DIW approaches have limitations for graphene 3D printing applications. Therefore, it is necessary to develop a new method for 3D printing of complex structures from graphene and its derivatives with any concentrations.

In this study, a nanoclay-assisted DIW technique is proposed to print 3D graphene structures. The low dispersion ability of graphene limits the formation of inks with the desired concentration of graphene [29]; hence, GO is selected as an exemplary graphene derivative because of its higher dispersing ability attributed to its hydrophilic functional groups. GO is graphene laced with oxygen-containing groups [36] with a two-dimensional structure similar to graphene [37]. GO is widely used in energy storage [38-40], corrosion resistance [41, 42], and stimuli response [43–45]. Pure GO colloid has low viscosity and poor printability. Thus, laponite nanoclay (Na_{0.7}Si₈Mg_{5.5}Li_{0.3}O₂₀(OH)₄) suspension is selected as the additive to improve the printability of GO colloids. Laponite nanoclay suspension is composed of numerous nanosilicates. When dispersed in an aqueous solution, sodium ions dissociate from each nanosilicate, leaving the faces with negative charges, while hydroxide ions dissociate from the edge, resulting in slight positive charges on the nanosilicate. The charge distribution enables laponite nanoclay to form a unique "house-of-cards" arrangement due to the electrostatic balance [46]. This specific nanoscale arrangement makes laponite nanoclay suspension possess yield-stress property in that it easily flows out of the dispensing nozzle, then rapidly supports itself after extrusion. Interestingly, when mixing with other matrix solutions, laponite nanoclay functions as an internal scaffold additive and the resulted nanocomposite suspensions inherit this yield-stress property and self-supporting capacity, making direct printing of complex liquid 3D structures in air feasible as reported in the previous studies [46, 47]. Thus, a GO-laponite nanocomposite is investigated as the ink for 3D printing applications. Herein, the extrudability of GO-laponite nanocomposites is characterized by their rheological properties and the nanocomposites with different laponite to GO mass ratios are studied. In addition, formability is explored by unveiling the effects of operating conditions and assessing the deflection of deposited filaments. Finally, complex 3D scaffolds are successfully printed based on the obtained knowledge, validating the effectiveness of the proposed 3D printing approach for the fabrication of graphene structures.



2 Materials and methods

2.1 Material preparation

Preparation of GO colloids GO was synthesized by the improved Hummers' method [48]. Expandable graphite flakes (CAS #12777876, > 50 mesh, Sigma-Aldrich, St. Louis, MO) of an appropriate amount were thermally expanded using a microwave oven for 30 s. The expanded graphite flakes were then transferred into an appropriate volume of concentrated H₂SO₄/H₃PO₄ mixture (9:1 in volume) and kept in an ice bath. After slowly adding a given amount of KMnO₄ into the mixture within 2 h, the solution was transferred to a 50 °C water bath and further stirred for 5 h. Finally, iced deionized (DI) water with H₂O₂ (30 wt.%) was prepared with the volume ratio of 150:1 and added into the solution. The obtained solution was repeatedly centrifuged with 1 M HCl solution and sequentially with DI water at 8000 rpm via centrifuge (BKC-TH21, Biobase Biotech (Jinan) Co., Ltd., Shandong, China) until the supernatant was neutral. The obtained GO paste was freeze-dried for 48 h and redispersed in DI water to produce GO colloids (10 mg/mL, sonicate for 1 h). Other colloids with different GO concentrations (2.5, 5.0, and 7.5 mg/mL) were diluted by adding DI water to the 10 mg/mL GO colloids without further sonication.

Preparation of GO-laponite nanocomposites Laponite RD nanoclay (BYK Additives Inc., Gonzales, TX) was used in this study. The appropriate amount of laponite powder was dispersed into GO colloids with different concentrations as shown in Table 1. Then, a vortex mixer (4ESS-MI0101002, Guangzhou Four E's Scientific Co., Ltd, Guangdong, China) was used to uniformly distribute the laponite powder in the colloids for 2 min. The obtained nanocomposites were moved to the centrifuge (CL4M, Waverly Scientific, Waverly, IA) at 3500 rpm for 10 min to remove entrapped air bubbles. All of the preparation steps were performed at room temperature under standard pressure. Nanocomposites with different laponite to GO mass ratios, as listed in Table 1, were prepared and sealed in dark for 24 h for aging before use, which were used for the extrudability characterization and formability investigation.

Table 1 Preparation of the nanocomposites with different laponite to GO mass ratios

No.	Laponite concentration % (w/v)	GO concentration (mg/mL)	Laponite to GO mass ratio
1	8.0	2.5	32.00
2	8.0	5.0	16.00
3	6.5	5.0	13.00
4	5.0	5.0	10.00
5	5.0	7.5	6.67
6	5.0	10.0	5.00

2.2 Printing system and printing protocols

An extrusion 3D printer (EFL-BP-6601, Suzhou Intelligent Manufacturing Research Institute, Suzhou, China) was used to perform all printing experiments at room temperature. During printing, the nanocomposite inks were fed into the 3D printer via high-pressure air. By extruding through a micro dispensing nozzle, continuous filaments were formed at the exit of the nozzle. With the movements of the print bed and printhead along horizontal and vertical directions respectively, filaments were deposited into 3D structures in a layer-by-layer manner.

For the formability investigation, a series of filament printing experiments were performed to investigate the effects of operating conditions including dispensing pressure, path speed, nozzle diameter, and stand-off distance on the filament shapes/dimensions on a substrate. First, different dispensing pressures (5, 6, and 7 psi (i.e., 3.45×10^4 , 4.14×10^4 , and 4.83 \times 10⁴ Pa)) were applied to extrude nanocomposite inks through a 20-gauge nozzle (inner diameter of about 600 µm) and the path speed and stand-off distance were set as 2 mm/s and 0.6 mm, respectively. Then, to understand the effects of path speed, the dispensing pressure was set as 6 psi (4.14 × 10⁴ Pa), the 20-gauge dispensing nozzle was used, and the stand-off distance was controlled as 0.6 mm, while the path speed was increased from 0.5 to 4.0 mm/s with an increment of 0.5 mm/s. After that, different dispensing nozzles (22gauge with an inner diameter of approximately 400 µm, 20gauge, and 18-gauge with an inner diameter of approximately 800 µm) were used for filament extrusion, while the dispensing pressure, path speed, and stand-off distance were kept as 7 psi $(4.83 \times 10^4 \text{ Pa})$, 2 mm/s, and 0.6 mm, respectively. Finally, the effects of stand-off distance were studied by setting the dispensing pressure as 6 psi $(4.14 \times 10^4 \text{ Pa})$, path speed as 2 mm/s, and nozzle diameter as 600 µm (20-gauge), while varying the stand-off distance from 0.4, 0.6, to 0.8 mm.

For the filament deflection investigation, a measuring tool was designed in SolidWorks (Dassault Systemes SolidWorks Corp., Waltham, MA) with a series of gaps between adjacent supporting structures and fabricated using an FDM 3D printer (Ender-3 Pro, Shenzhen Creality 3D Technology Co. Ltd., Shenzhen, China). The measuring tool had 8 gaps with the



increasing spacings from 0.5 to 4.0 mm and an increment of 0.5 mm. The nanocomposite with the laponite to GO mass ratio of 16.00 was used as the ink due to its superior extrudability and formability. When printing the filaments atop this measuring tool, the dispensing pressure, path speed, nozzle diameter, and stand-off distance were selected as 6.5 psi $(4.48 \times 10^4 \text{ Pa})$, 2 mm/s, 310 μ m (24-gauge), and 0.6 mm, respectively.

The same operating conditions were used for 3D printing of scaffolds from GO-laponite nanocomposites with a mass ratio of 16.00. The scaffold was designed with the overall dimensions of 11.25 mm \times 11.25 mm \times 4.50 mm, which had six layers, and each layer was composed of five uniformly distributed horizontal filaments. The distance between two adjacent filaments was 2.5 mm. After printing a layer, the printhead was moved along the vertical direction at a step distance of 350 μm to print the next layer by changing the trajectory direction perpendicular to the previous one.

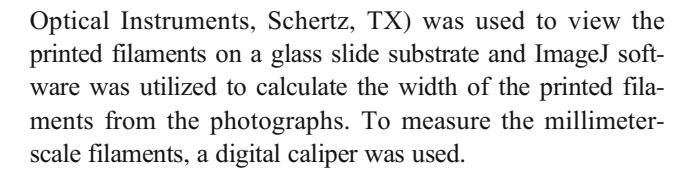
After 3D printing, the as-printed scaffolds were dried for 24 h at $-70\,^{\circ}$ C in a freeze dryer (BK-FD10S, Biobase Biotech (Jinan) Co., Ltd., Shandong, China) and then annealed at 700 $^{\circ}$ C for 2 h under argon atmosphere using tube furnace (OTF-1200X, MTI Corporation, California).

2.3 Rheological property measurements

Rheological properties of the nanocomposites were measured using a rheometer (MCR 92, Anton Paar GmbH, Graz, Austria) at room temperature. The cone-plate measuring system had a plate diameter of 50 mm, a cone angle 1.002°, and a cone-to-plate gap distance of 102 µm. First, steady shear rate sweeps were performed to determine the relationship between shear stress and shear rate and characterize the yield-stress property by varying the shear rate from 0.01 to 100 s⁻¹. Then, frequency sweeps were conducted to explore the storage modulus (G') and loss modulus (G") at different frequencies ranging from 0.1 to 100 rad/s at a low shear strain of 1.0% (this strain corresponded to the linear viscoelastic region of the nanocomposites). G' and G" were used to quantify the solidlike and liquid-like behaviors of the nanocomposites, respectively. Finally, transient sweeps were carried out to determine the repeatability of the nanocomposites to switch their states between liquid and solid-like. During testing, the nanocomposites were sheared at a low shear strain of 1.0% for 300 s and then at a high shear strain of 100.0% for another 300 s, repeating this process for 1500 s in total. Both G' and G" were recorded to characterize the liquid-solid-like transition at different shear strains.

2.4 Visualization and measurement of filaments

A microscope (SW380T, Swift Optical Instruments, Schertz, TX) with a digital camera (SC 1003, SWIFTCAM, Swift



2.5 Deflection evaluation

Filaments were printed over the measuring tool and the deflection depth at each spacing was imaged by a camera (PC 2275, Canon Inc., Tokyo, Japan). A home-made holder was designed in the lab to keep a constant distance between the measuring tool and the camera. The deflection in each image was measured using ImageJ.

2.6 Statistical analysis

All measurements and experiments were repeated 3 times and the quantitative values in the text and figures were reported as means \pm standard deviation (SD) with n=3 samples per group.

3 Extrudability investigation

The rheological properties determine the extrudability of the nanocomposites directly. Herein, the results of rheological property measurements are presented and the explanations behind different phenomena are discussed.

3.1 Results

Different rheological property measurements including steady shear rate sweeps, frequency sweeps, and transient sweeps were performed to the different nanocomposites with the laponite to GO mass ratios of 32.00, 16.00, 13.00, 10.00, 6.67, and 5.00. The results are illustrated in Fig. 1.

Figure 1a shows the relationship between shear stress and shear rate of the nanocomposites with different mass ratios. It is found that the shear stress of each nanocomposite increased with the increase of shear rate. The yield stress for each nanocomposite can be obtained by fitting the shear stress-shear rate data into the Herschel-Bulkley model [49]: $\tau = \tau_0 + k\dot{\gamma}^n$ where, τ is the shear stress, $\dot{\gamma}$ is the shear rate, τ_0 is the yield stress, k is the consistency index, and n is the flow index. This yield stress can be used to evaluate the self-supporting capacity of ink materials. As shown in Fig. 1a, the nanocomposite with the highest laponite to GO mass ratio of 32.00 presented the highest yield stress of 224.56 Pa. When the mass ratio decreased to 16.00, the yield stress of the corresponding nanocomposite decreased to 167.64 Pa. Further, the decrease of mass ratio from 13.00 to 10.00 resulted in the pronounced decrease of the yield stress from 33.77 to 11.25 Pa. When



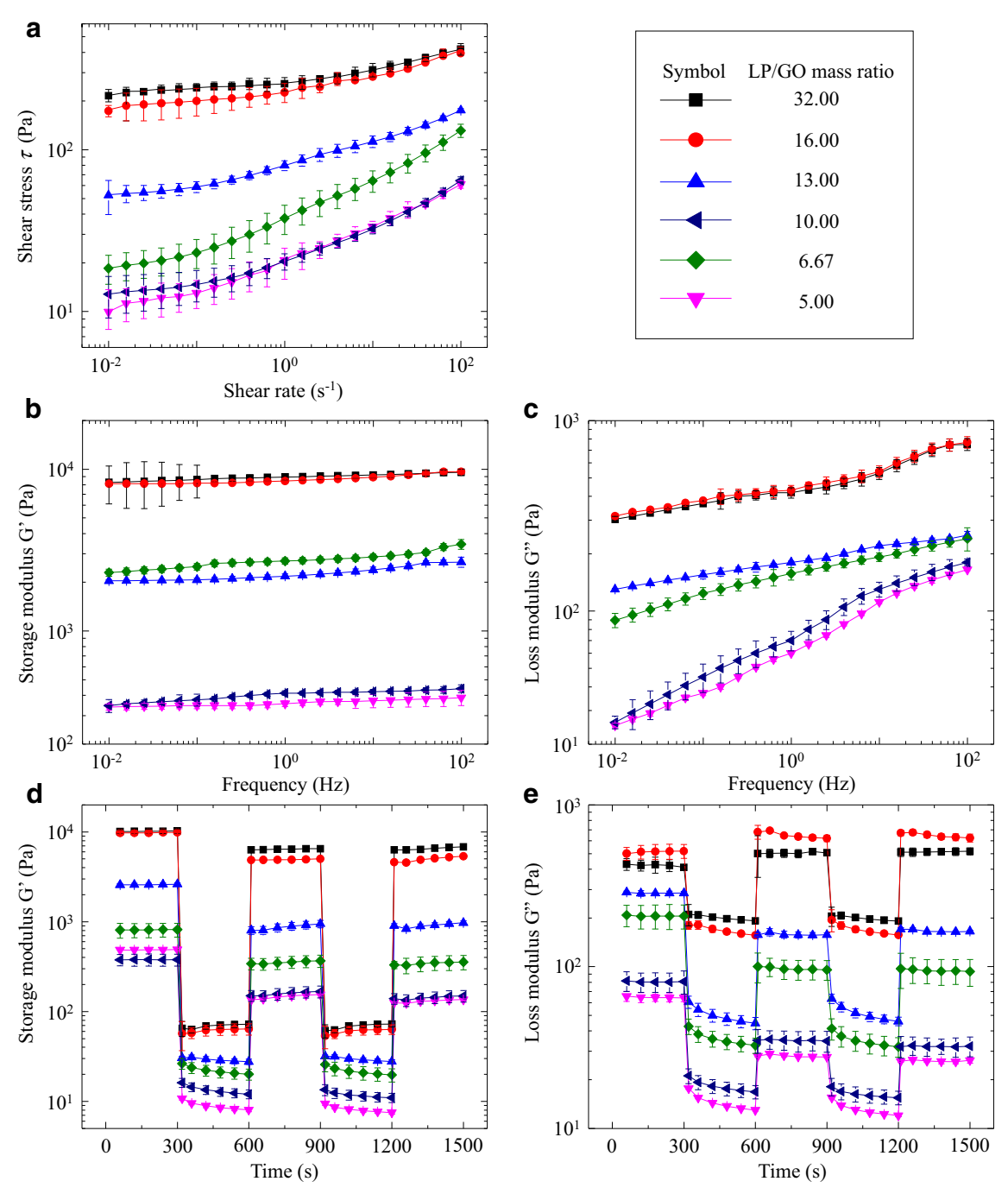


Fig. 1 Rheological property measurements of nanocomposites with different laponite (LP) to GO mass ratios. a Steady shear rate sweeps: shear stress as a function of shear rate. Frequency sweeps: b storage

modulus (G') and \boldsymbol{c} loss modulus (G'') as a function of frequency. Transient sweeps: \boldsymbol{d} storage modulus and \boldsymbol{e} loss modulus as a function of time

the mass ratio decreased from 10.00 to 5.00, the yield stress of the nanocomposites first increased to 13.26 Pa at the mass ratio of 6.67 and then decreased to 6.08 Pa at the mass ratio of 5.00. The mass ratio of 6.67 was the critical laponite to GO mass ratio in this range.

Then, frequency sweeps were carried out to determine the storage modulus (G') and loss modulus (G") of the nanocomposites with different laponite to GO mass ratios. The results

are illustrated in Fig. 1b and c, respectively. By comparing the storage modulus (Fig. 1b) with the loss modulus (Fig. 1c) of each nanocomposite, it is found that G' was greater than G", which indicated that these nanocomposites demonstrated solid-like behavior during shearing. In addition, shear moduli of the nanocomposites with higher mass ratios were independent on the mass ratio change. The nanocomposites with the mass ratios of 32.00 and 16.00 had nearly equivalent G' and



G". However, with the decrease of the mass ratio from 16.00 to 10.00, both G' and G" decreased. When the mass ratios of the nanocomposites decreased from 10.00 to 5.00, G' and G" first increased and then decreased, which were consistent with the yield-stress property results. The critical laponite to GO mass ratio was 6.67.

Finally, transient sweeps were used to determine the capacity of the nanocomposites with different laponite to GO mass ratios to frequently switch between liquid and solid-like states at different shear strains. The results are illustrated in Fig. 1d and e. It is observed that at a low shear strain of 1.0%, the storage modulus of each nanocomposite was higher than the loss modulus, indicating the solid-like behavior of the nanocomposite, while at a high shear strain of 100.0%, the loss modulus was higher than the storage modulus, illustrating the transition from solid-like to liquid. In addition, both G' and G" of each nanocomposite presented excellent repeatability during each strain decrease/increase cycle, which proved that the GO-laponite nanocomposites can rapidly and frequently switch between solid-like and liquid states.

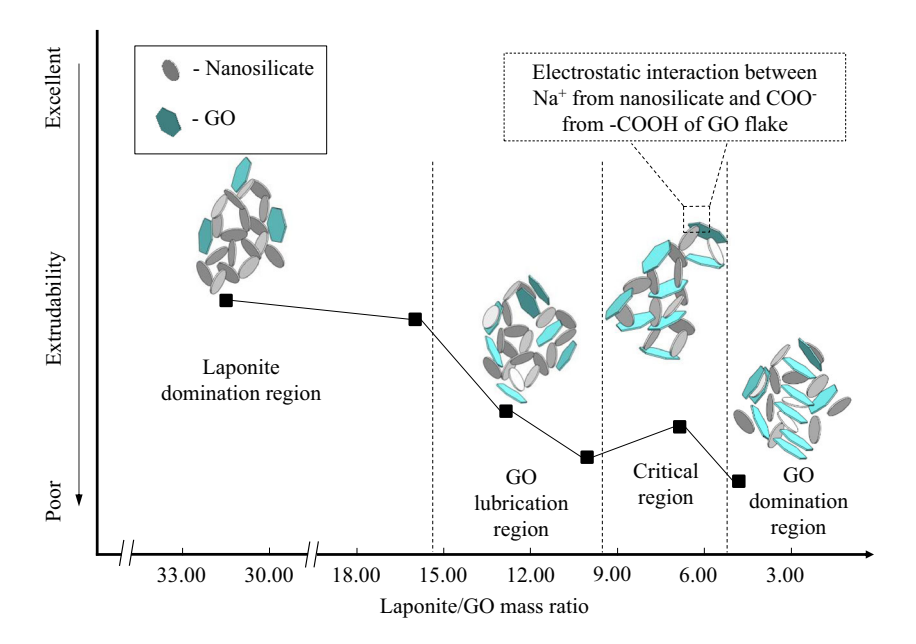
3.2 Discussions

From the aforementioned measurement results, it is found that the laponite to GO mass ratio can significantly affect the rheological properties of the nanocomposites, which further determines the extrudability of the nanocomposite inks. In this study, a significantly larger range of laponite to GO mass ratio (5.00 to 32.00) was provided by the vortex mixing and centrifugation method as compared to that (up to 10.00) of the solvent evaporation method reported previously [50]. Different phenomena with the change of mass ratios are summarized and explained in a phase diagram as shown in Fig. 2.

As seen from Fig. 2, there are four representative mass ratio regions: (1) laponite domination region, (2) GO lubrication region, (3) critical region, and (4) GO domination region. When dispersed in an aqueous-based solvent, hydroxide ions dissociate from the edges of nanosilicates and leave the edges with positive charges, while sodium ions dissociate from the surfaces of nanosilicates, leading to the negative charges on the surfaces [46, 47]. Thus, due to the electrostatic attraction between edges and surfaces, the instinctive "house-of-cards" arrangement is formed in the laponite nanoclay suspension. In the laponite domination region, the amount of GO flakes is limited which cannot change the extrudability significantly. In contrast, the large amount of nanosilicates can still form stable "house-of-cards" arrangement, dominating the extrudability. That explains why the decrease of laponite to GO mass ratio from 32.00 to 16.00 did not greatly affect the rheological properties of the nanocomposite inks as shown in Fig. 1. In this region, the nanocomposite inks present excellent selfsupporting property due to the relatively high yield stress values as well as good fluidability due to the shear-thinning property [51], which is defined as the decreasing viscosity with the increase of shear rate as illustrated by the slopes of shear stress-shear rate curves in Fig. 1a. Thus, the nanocomposite inks with the mass ratio in this region are promising to be used for 3D structure printing applications.

Decreasing the laponite to GO mass ratio increases the amount of GO flakes in the nanocomposite suspensions. In particular, when the mass ratio changes in the range of 16.00 to 10.00, more GO flakes insert into the "house-of-cards" arrangement. These GO flakes function as the lubricant to weaken the interactions between laponite nanosilicates during extrusion [29, 34], resulting in the significant decrease of the extrudability. Thus, this mass ratio range is named as "GO

Fig. 2 Phase diagram of the extrudability of the nanocomposites with different laponite to GO mass ratios





lubrication region," in which the rheological properties are sensitive to the change of laponite to GO mass ratios as shown in Fig. 1.

However, further decreasing the mass ratio from 10.00 to 6.67 does not result in a decrease in the rheological properties. In contrast, the shear stress, storage modulus, and loss modulus of the nanocomposite ink increase when the laponite to GO mass ratio is 6.67. This region is called "critical region," as shown in Fig. 2. This is due to the increasing amount of GO flakes in the nanocomposite provide sufficient carboxylate ions (COO⁻) from the carboxyl (-COOH) functional group in GO flakes, which can have an electrostatic attraction with sodium ions (Na⁺) from the nanosilicates [50, 52, 53]. This secondary electrostatic interaction leads to the formation of another stable microstructure, named GO-assisted "house-ofcards" arrangement, as shown in Fig. 2. As a result, the extrudability of the nanocomposite inks in the critical region is enhanced, which has the potential to be used for 3D printing purpose.

When the mass ratio decreases from 6.67 to 5.00, GO flakes still exist in the nanocomposites. The GO flakes form a GO-assisted "house-of-cards" arrangement, where more flakes can move freely in the suspensions during extrusion, serving as the lubricants. This mass ratio range is called "GO domination region," in which the rheological properties and extrudability can be shown to significantly decrease in Fig. 2.

4 Formability investigation

Formability, as aforementioned, is defined as the capacity of forming filaments on a substrate with controllable shapes and dimensions as well as the capacity of maintaining continuous filaments between supporting structures with negligible deflections. The former is mainly affected by the operating conditions including dispensing pressure, path speed, nozzle diameter, and stand-off distance as shown in Fig. 3, while the latter depends on the mechanical properties of the ink materials and geometries of the supporting structures. Herein, the nanocomposites with different laponite to GO mass ratios (32.00, 16.00, 13.00, 10.00, 6.67, and 5.00) were used as the

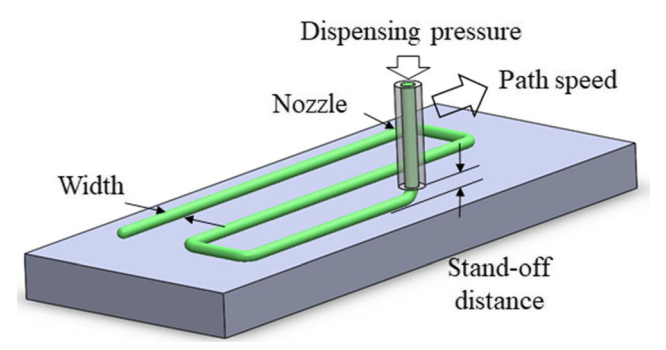


Fig. 3 Schematic of nanocomposite filament printing

ink materials to print filaments. The effects of the operating conditions on the filament width were first investigated and then the deflections of the filament atop the supporting structures were discussed.

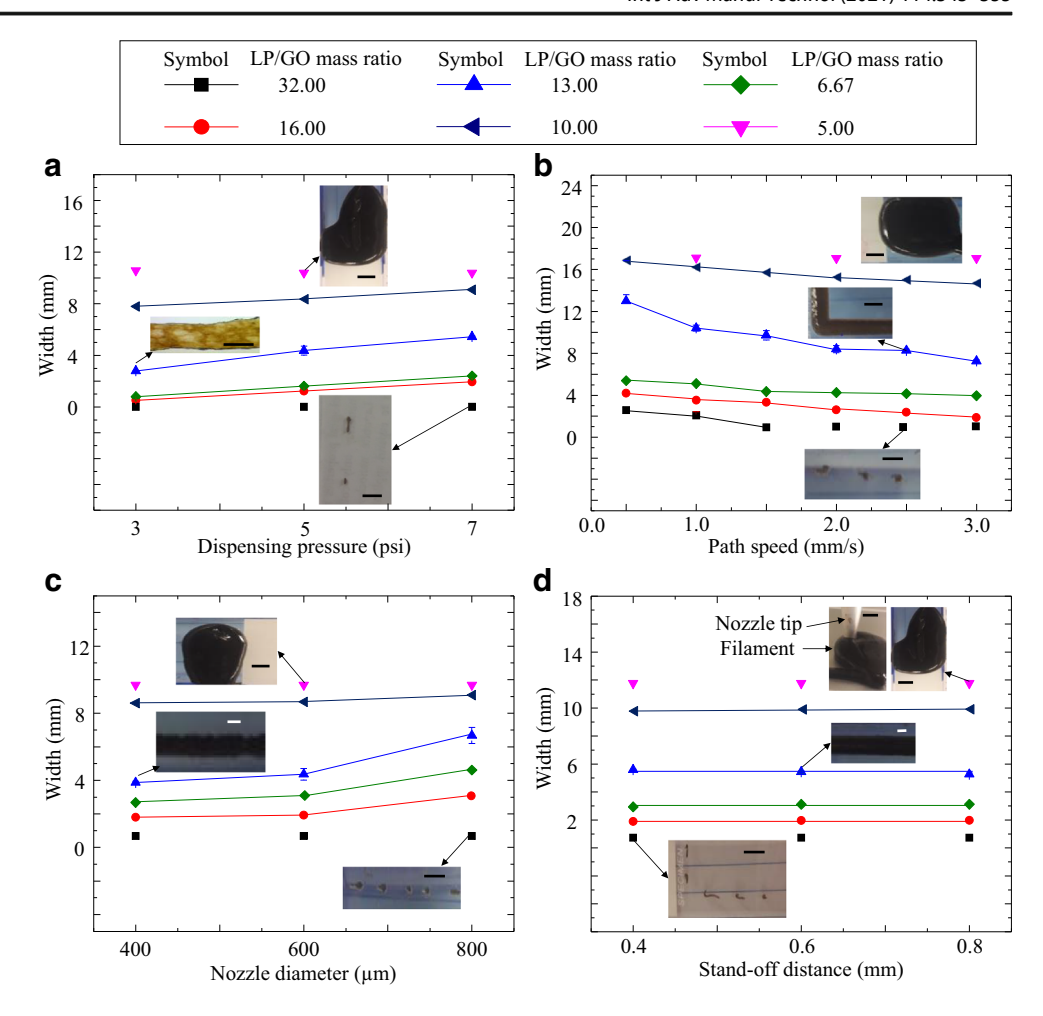
4.1 Effects of operating conditions

The effects of dispensing pressure on the filament width are illustrated in Fig. 4a. When the dispensing pressure increased, the filament width increased, which is consistent with the reported results [54, 55]. In addition, when the laponite to GO mass ratio was 32.00, due to the high yield stress of the nanocomposite ink and insufficient dispensing pressure, no continuous filaments were able to be extruded out of the dispensing nozzle. Instead, only some droplets/segments were observed on the receiving substrate as shown in the insets of Fig. 4a. However, with the decrease of the laponite to GO mass ratios, the yield stresses and viscosities of the nanocomposite inks decreased and continuous filaments can be formed on the substrate. From Fig. 4a, it is found that the filament width increased with the decreasing mass ratios, and the filament morphology changed from discontinuous filaments (droplets/segments), to well-defined filaments with controllable geometries. Finally, the well-defined filaments changed to over-deposited filaments [35] from the nanocomposite with the mass ratio of 5.00, which had uncontrollable dimensions as shown in the insets of Fig. 4a. It is noted that the width of the filaments from the nanocomposite with the mass ratio of 6.67 was much smaller than that from the nanocomposite with the mass ratio of 10.00. That is because the formation of GOassisted "house-of-cards" arrangement enhances the extrudability of the ink materials in the critical region and improves the filament diameter and morphology as shown in Fig. 2.

Path speed, which is also named as printing speed or feed rate, is defined as the speed at which the dispensing nozzle moves during ink material deposition. The filament morphology is not only affected by the applied path speed but also depends on the velocity of ink materials being extruded. From Fig. 4b, it is found that the width of the filament decreased with the increase of path speed. That is because the velocity of the extruded nanocomposites is constant at a given dispensing pressure. Thus, the dragging effect from the nozzle movement on the extruded filaments is pronounced with the increasing path speed, leading to the decrease of the filament width [38]. As seen from Fig. 4b, decreasing the laponite to GO mass ratio caused the decrease of viscosity, which resulted in the increase of the extrusion velocity of the nanocomposites. As a result, at the same path speed, the filaments from the nanocomposites with the lower laponite to GO mass ratios had the larger dimensions. In particular, when the mass ratio decreased to 5.00, the viscosity of the nanocomposite ink was too low and the extrusion velocity was too high to form well-defined filaments at any path speeds. Only over-deposited filaments can be



Fig. 4 Effects of operating conditions on the filament width. Filament width as a function of (a) dispensing pressure, (b) path speed, (c) nozzle diameter, and (d) stand-off distance (scale bars: 3.0 mm)



observed as shown in the insets of Fig. 4b. However, when the path speed was much higher than the extrusion velocity of the nanocomposites, the deposited filaments can break up into droplets/segments on the substrate due to the dragging effect as shown in the photographs of the filament printing results from the ink with the mass ratio of 32.00.

Nozzle diameter directly affects the dimensions of extruded filament. With the increasing nozzle diameter, the filament width increased as shown in Fig. 4c. From Fig. 4c, it is observed that for the nanocomposites with the higher laponite to GO mass ratio (such as 32.00), discontinuous filaments can be formed due to the insufficient dispensing pressure and small nozzle diameter (e.g., 0.4 mm). In contrast, for the nanocomposites with the lower mass ratio (e.g., 5.00), over-deposited filaments were formed due to the decreasing viscosity of the corresponding nanocomposites as shown in Fig. 4c. Thus, it is necessary to select suitable dispensing nozzles for various printing applications.

Stand-off distance is the distance between the nozzle tip and the receiving substrate as shown in Fig. 3. The filament widths printed at different stand-off distances are illustrated in Fig. 4d. It is found that the filament width was insensitive to the change of stand-off distances when some nanocomposite inks were used. For the nanocomposites with the laponite to

GO mass ratios of 16.00, 13.00, 10.00, and 6.67, the increase of stand-off distance resulted in the negligible effects on the filament width. That is because the prepared nanocomposites possess the yield-stress property due to the addition of laponite additives. Once extruded out of the nozzle, nanocomposite filaments rapidly switch their states from liquid to solidlike and stably maintain their cylindrical shapes with the diameter close to the nozzle inner diameter [38]. Thus, the width of the filament deposited on the substrate cannot change with the stand-off distance in the given range as shown in the insets of Fig. 4d. However, if the stand-off distance was smaller than the height of the deposited filament, more nanocomposites were extruded and stacked at the given location, leading to the formation of over-deposited filaments as shown in the insets of Fig. 4d for the nanocomposite with the mass ratio of 5.00. It is noted that for the nanocomposites with higher laponite to GO mass ratios (e.g., 32.00), limited amount of nanocomposites were observed to be extruded at the exit of the nozzle tip and discontinuous filaments were formed. That is because the nanocomposites with higher laponite to GO mass ratios usually have higher yield stresses and viscosities as shown in Fig. 1. Thus, higher dispensing pressure and/or larger nozzle are needed to facilicate the continuity of the



extrusion process. As a result, for 3D printing of the proposed nanocomposite inks, the primary requirement of the stand-off distance is that it must be larger than the height of the deposited filaments.

4.2 Filament deflections

One filament was deposited on top of the measuring tool with the increasing spacings as shown in Fig. 5a. The maximum deflection occurred in the middle of the spanning filament and the deflections were measured using ImageJ as shown in Fig. 5b. It is found that with the increase of the spacing between adjacent supporting structures, the maximum deflection increased from 250 to $1000~\mu m$. This filament on the measuring tool system can be modeled as a simply supported beam as shown in the inset of Fig. 5a. The filament between two adjacent supporting pillars only experiences uniformly distributed self-gravity load. Thus, the relationship between the maximum deflection (δ_{max}) and the spacing (L) can be modeled as:

$$\delta_{max} = 5\rho g L^4 / (96ER^2)$$

where, E is the Young's modulus, ρ is the density, g is the gravity acceleration, and R is the beam radius. From this model, it is also found that the maximum deflection increases with the spacing.

5 3D scaffold fabrication

Based on the obtained knowledge from the aforementioned chapters, a scaffold structure was designed and 3D printed. The post-printing and post-treatment dimensions were measured and analyzed to prove the feasibility and effectiveness of the proposed fabrication approach to print complex 3D

structures with controllable geometries from GO-laponite nanocomposites.

5.1 3D scaffold printing

The 3D scaffold was designed as shown in Fig. 6a. Since the filaments for scaffold printing had a diameter of around 750 μ m, regarding the inter-filament conflicts and acceptable deflection, the spacing distance between adjacent filaments was designed as 2.5 mm, which corresponded to the deflection of 700 μ m as shown in Fig. 5b. Thus, the key dimensions of the designed scaffold are listed in Table 2.

Due to excellent printability, the nanocomposite with the laponite to GO mass ratio of 16.00 was selected as the ink for 3D scaffold printing and the result is illustrated in Fig. 6b. It is found that the printed scaffold had a well-defined shape and negligible filament deflections as shown in the top/front views of Fig. 6b. All of the key dimensions were measured using ImageJ and the relative errors are calculated by the following equation:

$$Error\left(\%\right) = \left|\begin{array}{c} measured\ dimension-designed\ dimension \\ designed\ dimension \times 100\% \end{array}\right|$$

Thus, the comparisons between the designed dimensions and the measurements are summarized in Table 2. It is found that the relative errors of all key dimensions were less than 15%, which means the printed structure had the geometries close to the designed ones. The slight decrease of the dimensions may be attributed to the water evaporation after printing, leading to the shrinkage of different dimensions. In addition, the measured deflection was around 0.79 mm, which was a little larger than the value measured on the measuring tool. This phenomenon can be explained by the flexible supports provided by the soft filaments in the scaffold instead of the rigid supports offered by the plastic measuring tool.

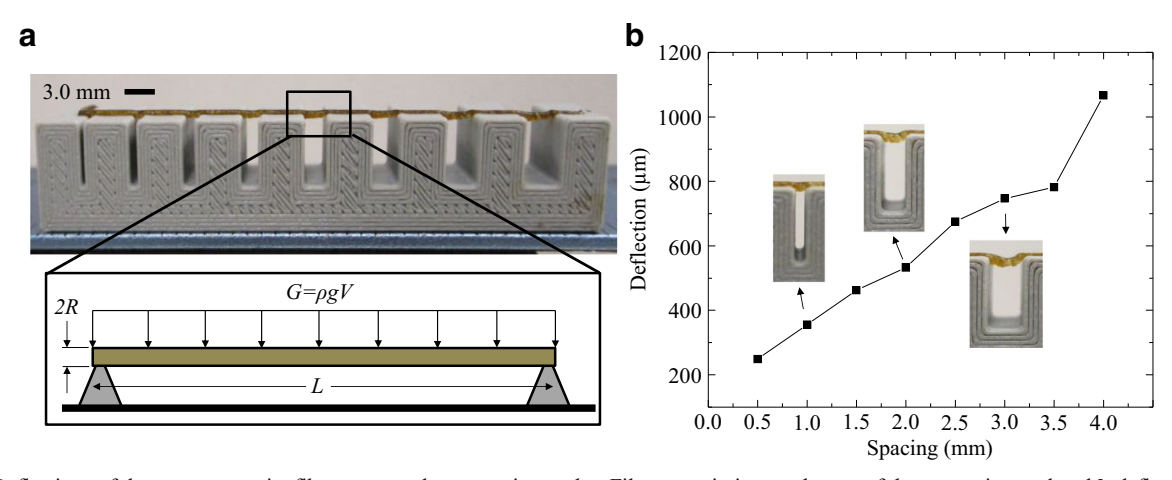


Fig. 5 Deflections of the nanocomposite filament atop the measuring tool. a Filament printing on the top of the measuring tool and b deflection as a function of spacing distance



Table 2	Comparison	between	the	designed	and	measured	dimensions
of the 3D	scaffold						

Scaffold design		After printing		After post-treatments		
Parameters	Values (mm)	Measured value (mm)	Error (%)	Measured value (mm)	Error (%)	
Length	11.25	10.21 ± 0.03	9.24	10.18 ± 0.01	9.51	
Width	11.25	10.52 ± 0.04	6.49	10.46 ± 0.02	7.02	
Height	4.50	4.03 ± 0.07	10.44	3.91 ± 0.05	13.11	
Spacing	2.50	2.23 ± 0.10	10.80	2.21 ± 0.01	11.6	
Deflection	0.00	0.79 ± 0.07	N/A	0.80 ± 0.01	N/A	
Diameter	0.75	0.73 ± 0.01	2.67	0.72 ± 0.02	2.25	

5.2 Analysis of 3D scaffolds after post-treatments

Post-treatments of the 3D scaffolds were performed to obtain the solid nanocomposite scaffolds as shown in Fig. 7, and the dimensions were measured as shown in Table 2. Table 2 shows that relative errors of the key dimensions of the scaffolds after post-treatments were still less than 15%. These slight dimensional differences before and after post-treatments can be explained from two aspects: (1) the freeze-drying process rapidly removes water molecules in the nanocomposite, but stably maintains the spatial distribution of the nanoclay particles and GO flakes in situ. Thus, the resulted scaffolds can keep the same macroscopic geometries with significant microscopic porosity [12, 55, 56]. (2) In the subsequent annealing process, the uniformly dispersed GO flakes function as anti-shrinkage additives, which can effectively reduce the shrinkage of the nanocomposite scaffolds as reported in the published papers [57, 58]. As a result, the nanocomposite structures fabricated by the proposed nanoclay-assisted 3D printing



Top view Front view

Fig. 7 Printed 3D scaffold after post-treatments (scale bars: 3.0 mm)

approach have a relatively high shape accuracy and can be used directly for various practical applications.

6 Conclusions and future work

In this study, extrudability has been investigated by characterizing the rheological properties of GO-laponite nanocomposites with different laponite to GO mass ratios. Then, formability has been studied by characterizing the filament width on the substrate as well as the filament deflections atop the measuring tool. Finally, based on the obtained knowledge, 3D scaffolds with well-defined shapes and controllable geometries have been successfully 3D printed. The main conclusions of this study are summarized as follows:

1. With the decrease of laponite to GO mass ratio, there are four representative regions corresponding to different extrudabilities. In the laponite domination region, the

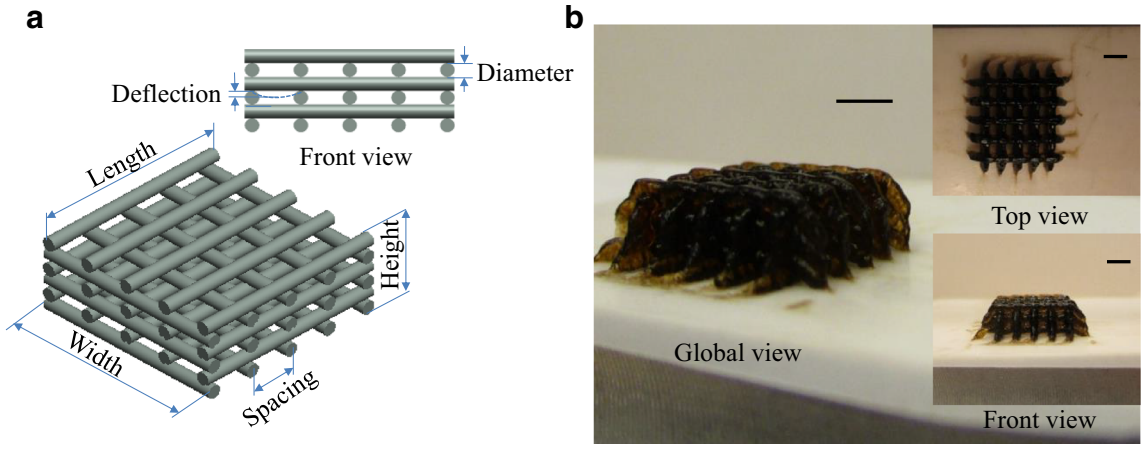


Fig. 6 a Schematic of designed 3D scaffold and b printed 3D scaffold before post-treatments (scale bars: 3.0 mm)



- nanocomposite inks have the best extrudability, while the extrudability in the critical region has the potential to be used for 3D printing purpose;
- 2. Operating conditions can affect the filament width directly. The filament width on the substrate increases with the increase of both the dispensing pressure and nozzle diameter. The filaments width decreases with the increase of the path speed. The filament width is insensitive to the change of stand-off distance as long as the stand-off distance is larger than the filament height on the substrate;
- 3. The filament deflection mainly depends on the spacing between adjacent supporting structures. For GO-laponite nanocomposite printing, when the spacing increases from 0.5 to 4.0 mm, the maximum deflection increases from 250 to 1000 μm; and
- 4. The relative errors of the dimensions of the scaffold structure after printing and post-treatments are both less than 15%, which indicates that the geometries of the achieved solid scaffolds are close enough to the designed values.

It is noted that laponite was not removed from the printed scaffolds. That is because laponite was reported to have the function of improving mechanical properties [46]. Thus, future work may focus on the characterization of the mechanical and electrical properties of the printed 3D structures from the proposed GO-laponite nanocomposites. In addition, to further enhance the mechanical stiffness of the printed 3D structures, other components such as poly(ethylene glycol) diacrylate will be added to the proposed nanocomposites as chemical crosslinkers and the effects of these chemical crosslinkers on the printability will be investigated in the future.

Acknowledgements The authors acknowledge the University of Nevada, Reno, for the financial support. A portion of this research was conducted at the Center for Nanophase Materials Sciences, which is a DOE Office of Science User Facility.

Code availability The G-code for scaffold printing is available upon request (email: yifeij@unr.edu).

Author contribution Y.J. conceived the concept of this work, M.S. conducted the rheological property measurements and printing experiments, S.T. prepared the GO colloids and did the post-treatments, J.C. analyzed the functionality of laponite and GO additives, L.R. and G.X. proofread the manuscript, and M.S., L.R., and Y.J. wrote the manuscript.

Funding This research was funded by the National Science Foundation (Grant No. CMMI-1923033).

Data availability The data presented here are available upon request (email: yifeij@unr.edu).

Declarations

Competing interests The authors declare no competing interests.

References

- Meyer JC, Geim AK, Katsnelson MI, Novoselov KS, Booth TJ, Roth S (2007) The structure of suspended graphene sheets. Nature 446:60–63. https://doi.org/10.1038/nature05545
- Sadhukhan S, Ghosh TK, Rana D, Roy I, Bhattacharyya A, Sarkar G, Chakraborty M, Chattopadhyay D (2016) Studies on synthesis of reduced graphene oxide (RGO) via green route and its electrical property. Mater Res Bull 79:41–51. https://doi.org/10.1016/j. materresbull.2016.02.039
- Papageorgiou DG, Kinloch IA, Young RJ (2017) Mechanical properties of graphene and graphene-based nanocomposites. Prog Mater Sci 90:75–127. https://doi.org/10.1016/j.pmatsci.2017.07.004
- Yang J, Zhou Y, Sun L, Zhao N, Zang C, Cheng X (2012) Synthesis, characterization and optical property of graphene oxide films. Appl Surf Sci 258:5056–5060. https://doi.org/10.1016/j. apsusc.2012.01.105
- Balandin AA, Ghosh S, Bao W, Calizo I, Teweldebrhan D, Miao F, Lau CN (2008) Superior thermal conductivity of single-layer graphene. Nano Lett 8:902–907. https://doi.org/10.1021/ nl0731872
- Kuila T, Mishra AK, Khanra P, Kim NH, Lee JH (2013) Recent advances in the efficient reduction of graphene oxide and its application as energy storage electrode materials. Nanoscale 5:52–71. https://doi.org/10.1039/c2nr32703a
- Xu Y, Sheng K, Li C, Shi G (2010) Self-assembled graphene hydrogel via a one-step hydrothermal process. ACS Nano 4:4324
 4330. https://doi.org/10.1021/nn101187z
- Zhang Q, Xu X, Lin D, Chen W, Xiong G, Yu Y, Fisher TS, Li H (2016) Hyperbolically patterned 3D graphene metamaterial with negative Poisson's ratio and superelasticity. Adv Mater 28:2229–2237. https://doi.org/10.1002/adma.201505409
- Li Y, Chen J, Huang L, Li C, Hong JD, Shi G (2014) Highly compressible macroporous graphene monoliths via an improved hydrothermal process. Adv Mater 26:4789–4793. https://doi.org/ 10.1002/adma.201400657
- Zhang P, Li J, Lv L, Zhao Y, Qu L (2017) Vertically aligned graphene sheets membrane for highly efficient solar thermal generation of clean water. ACS Nano 11:5087–5093. https://doi.org/10. 1021/acsnano.7b01965
- Wang C, Chen X, Wang B, Huang M, Wang B, Jiang Y, Ruoff RS (2018) Freeze-casting produces a graphene oxide aerogel with a radial and centrosymmetric structure. ACS Nano 12:5816–5825. https://doi.org/10.1021/acsnano.8b01747
- Qiu L, Liu JZ, Chang SLY, Wu Y, Li D (2012) Biomimetic superelastic graphene-based cellular monoliths. Nat Commun 3: 1241. https://doi.org/10.1038/ncomms2251
- Zhang X, Sui Z, Xu B, Yue S, Luo Y, Zhan W, Liu B (2011) Mechanically strong and highly conductive graphene aerogel and its use as electrodes for electrochemical power sources. J Mater Chem 21:6494–6497. https://doi.org/10.1039/C1JM10239G
- Hu H, Zhao Z, Wan W, Gogotsi Y, Qiu J (2013) Ultralight and highly compressible graphene aerogels. Adv Mater 25:2219–2223. https://doi.org/10.1002/adma.201204530
- Chen Z, Ren W, Gao L, Liu B, Pei S, Cheng HM (2011) Threedimensional flexible and conductive interconnected graphene networks grown by chemical vapour deposition. Nat Mater 10:424– 428. https://doi.org/10.1038/nmat3001
- ASTM International (2012) F2792-12a standard terminology for additive manufacturing technologies. ASTM International, West Conshohocken, PA
- You X, Yang J, Feng Q, Huang K, Zhou H, Hu J, Dong S (2018) Three-dimensional graphene-based materials by direct ink writing method for lightweight application. Int J Lightweight Mater Manuf 1:96–101. https://doi.org/10.1016/j.ijlmm.2018.05.003



- Maurel A, Courty M, Fleutot B, Tortajada H, Prashantha K, Armand M, Grugeon S, Panier S, Dupont L (2018) Highly loaded graphite–polylactic acid composite-based filaments for lithium-ion battery three-dimensional printing. Chem Mater 30:7484–7493. https://doi.org/10.1021/acs.chemmater.8b02062
- Wei X, Li D, Jiang W, Gu Z, Wang X, Zhang Z, Sun Z (2015) 3D printable graphene composite. Sci Rep 5:11181. https://doi.org/10.1038/srep11181
- Kim JH, Chang WS, Kim WS, Yang JR, Han JT, Lee GW, Kim JT, Seol SK (2014) 3D printing of reduced graphene oxide nanowires. Adv Mater 27:157–161. https://doi.org/10.1002/adma.201404380
- Das S, Pati F, Choi YJ, Rijal G, Shim JH, Kim SW, Ray AR, Cho DW, Ghosh S (2015) Bioprintable, cell-laden silk fibroin–gelatin hydrogel supporting multilineage differentiation of stem cells for fabrication of three-dimensional tissue constructs. Acta Biomater 11:233–246. https://doi.org/10.1016/j.actbio.2014.09.023
- Zhang T, Yan KC, Ouyang L, Sun W (2013) Mechanical characterization of bioprinted in vitro soft tissue models. Biofabrication 5: 045010. https://doi.org/10.1088/1758-5082/5/4/045010
- Gao Q, He Y, Fu J, Liu A, Ma L (2015) Coaxial nozzle-assisted 3D bioprinting with built-in microchannels for nutrients delivery. Biomaterials 61:203–215. https://doi.org/10.1016/j.biomaterials. 2015.05.031
- Melchels FPW, Dhert WJA, Hutmacher DW, Malda J (2014) Development and characterization of a new bioink for additive tissue manufacturing. J Mater Chem B 2:2282–2289. https://doi. org/10.1039/C3TB21280G
- Hong S, Sycks D, Chan HF, Lin S, Lopez GP, Guilak F, Leong KW, Zhao X (2015) 3D printing of highly stretchable and tough hydrogels into complex, cellularized structures. Adv Mater 27: 4035–4040. https://doi.org/10.1002/adma.201501099
- Wüst S, Godla ME, Müller R, Hofmann S (2014) Tunable hydrogel composite with two-step processing in combination with innovative hardware upgrade for cell-based three-dimensional bioprinting. Acta Biomater 10:630–640. https://doi.org/10.1016/j.actbio.2013. 10.016
- Lewis JA (2006) Direct ink writing of 3D functional materials. Adv Funct Mater 16:2193–2204. https://doi.org/10.1002/adfm. 200600434
- Naficy S, Jalili R, Aboutalebi SH, Gorkin RA III, Konstantinov K, Innis PC, Spinks GM, Poilin P, Wallace GG (2014) Graphene oxide dispersions: tuning rheology to enable fabrication. Mater Horiz 1: 326–331. https://doi.org/10.1039/C3MH00144J
- Ling S, Kang W, Tao S, Zhang C (2019) Highly concentrated graphene oxide ink for facile 3D printing of supercapacitors. Nano Mater Sci 1:142–148. https://doi.org/10.1016/j.nanoms. 2019.05.003
- Yao B, Chandrasekaran S, Zhang J, Xiao W, Qian F, Zhu C, Duoss EB, Spadaccini CM, Worsley MA, Li Y (2019) Efficient 3D printed pseudocapacitive electrodes with ultrahigh MnO₂ loading. Joule 3: 459–470. https://doi.org/10.1016/j.joule.2018.09.020
- Yao B, Chandrasekaran C, Zhang H, Ma A, Kang J, Zhang L, Lu X, Qian F, Zhu C, Duoss EB, Spadaccini CM, Worsely MA, Li Y (2020) 3D-printed structure boosts the kinetics and intrinsic capacitance of pseudocapacitive graphene aerogels. Adv Mater 32: 1906652. https://doi.org/10.1002/adma.201906652
- Zhu C, Han TY, Duoss EB, Golobic AM, Kuntz JD, Spadaccini CM, Worsley MA (2015) Highly compressible 3D periodic graphene aerogel microlattices. Nat Commun 6:6962. https://doi. org/10.1038/ncomms7962
- Tuñon EG, Barg S, Franco J, Bell R, Eslava S, Elia ED, Maher RC, Guitian F, Saiz E (2015) Printing in three dimensions with graphene. Adv Mater 27:1688–1693. https://doi.org/10.1002/ adma.201405046
- Yao Y, Fu KK, Yan C, Dai J, Chen Y, Wang Y, Zhang B, Hitz E, Hu L (2016) Three-dimensional printable high-temperature and

- high-rate heaters. ACS Nano 10:5272–5279. https://doi.org/10.1021/acsnano.6b01059
- Jakus AE, Secor EB, Rutz AL, Jordan SW, Hersam MC, Shah RN (2015) Three-dimensional printing of high-content graphene scaffolds for electronic and biomedical applications. ACS Nano 9: 4636–4648. https://doi.org/10.1021/acsnano.5b01179
- Lee XJ, Billie BYZ, Lai KC, Lee LY, Gan S, Thangalazhy-Gopakumar S, Rigby S (2019) Review on graphene and its derivatives: synthesis methods and potential industrial implementation. J Taiwan Inst Chem Eng 98:163–180. https://doi.org/10.1016/j.jtice. 2018.10.028
- Dideikin AT, Vul' AY (2019) Graphene oxide and derivatives: the place in graphene family. Front Phys 6. https://doi.org/10.3389/ fphy.2018.00149
- Wang M, Duong LD, Mai NT, Kim S, Kim Y, Seo H, Kim YC, Jang W, Lee Y, Suhr J, Nam J (2015) All-solid-state reduced graphene oxide supercapacitor with large volumetric capacitance and ultralong stability prepared by electrophoretic deposition method. ACS Appl Mater Interfaces 7:1348–1354. https://doi.org/10. 1021/am507656q
- Chee WK, Lim HN, Harrison I, Chong KF, Zainal Z, Ng CH, Huang NM (2015) Performance of flexible and binderless polypyrrole/graphene oxide/zinc oxide supercapacitor electrode in a symmetrical two-electrode configuration. Electrochimica Acta 157:88–94. https://doi.org/10.1016/j.electacta.2015.01.080
- Huang JQ, Zhuang TZ, Zhang Q, Peng HJ, Chen CM, Wei F (2015) Permselective graphene oxide membrane for highly stable and antiself-discharge lithium-sulfur batteries. ACS Nano 9:3002–3011. https://doi.org/10.1021/nn507178a
- Luo X, Zhong J, Zhou Q, Du S, Yuan S, Liu Y (2018) Cationic reduced graphene oxide as self-aligned nanofiller in the epoxy nanocomposite coating with excellent anticorrosive performance and its high antibacterial activity. ACS Appl Mater Interfaces 10: 18400–18415. https://doi.org/10.1021/acsami.8b01982
- Ghauri FA, Raza MA, Baig MS, Ibrahim S (2017) Corrosion study of the graphene oxide and reduced graphene oxide-based epoxy coatings. Mater Res Express:4. https://doi.org/10.1088/2053-1591/aa9aac
- Ma M, Guo L, Anderson DG, Langer R (2013) Bio-inspired polymer composite actuator and generator driven by water gradients. Science 339:186–189. https://doi.org/10.1126/science.1230262
- Lian Y, Liu Y, Jiang T, Shu J, Lian H, Cao M (2010) Enhanced electromechanical performance of graphite oxide-nafion nanocomposite actuator. J Phys Chem C 14:9659–9663. https://doi.org/10. 1021/jp101337h
- Zhao Q, Liang Y, Ren L, Yu Z, Zhang Z, Ren L (2018) Bionic intelligent hydrogel actuators with multimodal deformation and locomotion. Nano Energy 51:621–631. https://doi.org/10.1021/ acsami.7b0361310.1016/j.nanoen.2018.07.025
- Jin Y, Liu C, Chai W, Compaan A, Huang Y (2017) Self-supporting nanoclay as internal scaffold material for direct printing of soft hydrogel composite structures in air. ACS Appl Mater Interfaces 9:17456–17465. https://doi.org/10.1021/acsami.7b03613
- Jin Y, Shen Y, Yin J, Qian J, Huang Y (2018) Nanoclay-based selfsupporting responsive nanocomposite hydrogels for printing applications. ACS Appl Mater Interfaces 10:10461–10470. https://doi. org/10.1021/acsami.8b00806
- Marcano DC, Kosynkin DV, Berlin JM, Sinitskii A, Sun Z, Slesarev A, Alemany LB, Lu W, Tour JM (2010) Improved synthesis of graphene oxide. ACS Nano 4:4806–4814. https://doi.org/10.1021/nn1006368
- Burgos GR, Alexandrou AN, Entov V (1999) On the determination of yield surfaces in Herschel-Bulkley fluids. J Rheol 43:463–483. https://doi.org/10.1122/1.550992



- Chouhan DK, Patro TU, Harikrishan G, Kumar S, Gupta S, Kumar GS, Cohen H, Wagner HD (2016) Graphene oxide-laponite hybrid from highly stable aqueous dispersion. Appl Clay Sci 132:105–113. https://doi.org/10.1016/j.clay.2016.05.023
- Żołek-Tryznowska Z (2015) Rheology of printing inks. In: Izdebska J, Thomas S (eds) Printing on polymers: fundamentals and applications, 1st edn. Elsevier, Amsterdam, pp 87–99
- Chouhan DK, Kumar A, Rath SK (2018) Laponite-graphene oxide hybrid particulate filler enhances mechanical properties of crosslinked epoxy. J Polym Res 25. https://doi.org/10.1007/s10965-018-1461-2
- Yoo J, Lee SB, Lee CK, Hwang SW, Kim C, Fujigaya T, Nakashima N, Shim JK (2014) Graphene oxide and laponite composite films with high oxygen-barrier properties. Nanoscale 18: 10824–10830. https://doi.org/10.1039/c4nr03429e
- Jin Y, Chai W, Huang Y (2017) Printability study of hydrogel solution extrusion in nanoclay yield-stress bath during printingthen-gelation biofabrication. Mater Sci Eng C 80:313–325. https://doi.org/10.1016/j.msec.2017.05.144

- Habib A, Sathish V, Mallik S, Khoda B (2018) 3D printability of alginate-carboxymethyl cellulose hydrogel. Mater Basel Switz 11. https://doi.org/10.3390/ma11030454
- Habib MA, Khoda B (2018) Development of clay based novel bioink for 3D bio-printing process. Procedia Manuf 26:846–856. https://doi.org/10.1016/j.promfg.2018.07.105
- Guo K, Song H, Chen X, Du X, Zhong L (2014) Graphene oxide as an anti-shrinkage additive for resorcinol-formaldehyde composite aerogels. Phys Chem Chem Phys 16:11603–11608. https://doi.org/ 10.1039/C4CP00592A
- Tan L, Gan L, Hu J, Zhu Y, Han J (2015) Functional shape memory composite nanofibers with graphene oxide filler. Compos Part Appl Sci Manuf 76:115–123. https://doi.org/10.1016/j.compositesa. 2015.04.015

Publisher's note Springer Nature remains neutral with regard to jurisdictional claims in published maps and institutional affiliations.

